Thermals in the Numerical Laboratory

Ulrich Wölfel
ulrich.woelfel@gmail.com
wölfel consulting interimsmanagement
Edemissen, Germany

Abstract

The atmospheric boundary layer in blue thermal conditions is investigated by means of Large Eddy Simulation (LES) on a personal computer, in model cases of increasing (but limited by computing capacity) complexity. Despite the high idealization, and without large-scale forcing other than geostrophic wind in the free atmosphere, the resulting flow patterns match with aeronautical practice and literature. Strong thermals are joined by small thermals, originating from illuminated slopes and asphalt surfaces on the ground. Weaker thermals emanate from vegetation areas at a sufficient distance from asphalt. The drier the ground and the lower the transpiration of the vegetation, the stronger the thermals. Above forests, thermals are stronger than above grass surfaces. In the absence of wind, air sinks over water bodies.

Nomenclature

c_p	Heat capacity at constant pressure
$\frac{d}{dt}$	Substantial derivative
$\frac{\partial}{\partial t}$	Local derivative
∇	Nabla, gradient operator $(\frac{\partial}{\partial x}, \frac{\partial}{\partial y}, \frac{\partial}{\partial z})$
e	Mass-specific kinetic energy, also referred to as $u2$ in LES results
$\mathbf{F}_c$	Coriolis force vector
g	Gravitational acceleration
$\mathbf{k}$	Vertical unit vector
p'	Fluctuation pressure
q	Water vapor mixing ratio
u	Mass-specific internal energy
$\mathbf{v}$	Velocity vector
vnap	Pressure gradient transport term in specific kinetic energy budget equation
w	Vertical velocity component
x, y, z	Spatial coordinates, z is vertical
ρ	Density
pt_{flux}	Buoyancy term in specific kinetic energy budget equation
ν	Molecular viscosity
θ	Potential temperature
θ_v	Virtual potential temperature
$\Delta\theta$	Excess temperature compared with respect to boundary layer minimum

Symbol modifiers

$\overline{\theta}$	Horizontal mean of θ
θ'	Deviation from horizontal mean of θ
θ''	Sub-grid scale component of θ
θ^*	Resolved scale component of θ

Introduction and Theory

In the past, various considerations have been made about the nature of thermals, partly experimentally [1–4], in motor gliders, gliders, and from the ground, and partly theoretically [5]. In this paper, a theoretical approach is pursued, initially based on the Navier-Stokes equations and considering the kinetic energy of the total flow and turbulence.

Thermals distribute the energy from solar irradiation onto the earth's surface into the atmosphere. Accordingly, we conduct an energy balance analysis, following [6–8]. There are temperature differences θ' relative to the horizontal mean $\overline{\theta}$, as well as an excess temperature $\Delta\theta$ relative to the boundary layer minimum. This excess temperature corresponds to a mass-specific internal energy u (with ρ as density and c_p as heat capacity at constant pressure):

$$u = \rho c_p \Delta\theta. \tag{1}$$

To investigate kinetic energy, we use the momentum equations in the Boussinesq approximation. Consider a horizontally homogeneous basic state at rest, without mean flow in any direction:

$$\frac{d\mathbf{v}}{dt} = -\frac{1}{\rho}\nabla p' + \mathbf{F}_c + g\frac{\theta'}{\theta}\mathbf{k} + \nu\nabla^2\mathbf{v}. \tag{2}$$

Here $\frac{d}{dt}$ is the substantial derivative (Lagrangian/material view as moving with the air parcel), bold face $\mathbf{v}$ is the velocity

This article was peer reviewed by two independent, anonymous reviewers.

vector, ∇ the gradient operator, p' the fluctuation pressure, $\mathbf{F}_c$ the Coriolis force, g the gravitational acceleration, $\mathbf{k}$ the vertical unit vector, and ν the molecular viscosity. Superscript (e.g. θ') indicates a local deviation of potential temperature from its horizontal mean $\overline{\theta}$. Scalar multiplication with $\mathbf{v}$ results in a budget equation for the total specific kinetic energy e (later referenced as $u2$):

$$\frac{de}{dt} = -\frac{1}{\overline{\rho}}\mathbf{v}\cdot\nabla p' + g\frac{\theta'}{\overline{\theta}}w + \nu\nabla^2 e - \nu\left(\frac{\partial v_i}{\partial x_j}\right)^2. \qquad (3)$$

Specific kinetic energy of an air parcel is subject to change either by pressure gradient transport (first term, later referenced as vnap) and by buoyancy (second term, pt_{flux}). The third diffusive term can generate kinetic energy, at its spatial minima, or destroy it, at the maxima. The last term is loss by molecular dissipation. The last two contain the (small) molecular viscosity, however in small scale structures they may be significant. It is emphasized that buoyancy increases kinetic energy proportionally not only to temperature excess θ', but to its product with vertical velocity w, if both are either positive or negative!

With the Boussinesq approximation, the continuity equation is:

$$\nabla\cdot\mathbf{v} = 0. \qquad (4)$$

These equations are valid locally and instantaneously, moving with an air parcel. They allow analyzing instantaneous calculation results of the evolution of convection, the thermals.

Many textbooks [6, 8] investigate turbulence after averaging. Eulerian view (in a locally fixed reference frame) of mean *turbulent* kinetic energy $\overline{e}$, the difference between total kinetic energy e and that of any base flow, combined with a deformation approach for $\overline{v_i'v_j'}$ results in [6]:

$$\frac{\partial\overline{e}}{\partial t} + Div = \frac{K}{2}\left(\frac{\partial\overline{v}_i}{\partial x_j} + \frac{\partial\overline{v}_j}{\partial x_i}\right)^2 + \frac{g}{\overline{\theta}}\overline{\theta'w'} - \nu\overline{\left(\frac{\partial v_i'}{\partial x_j}\right)^2}, \qquad (5)$$

in tensor terminology. K is the turbulent diffusion coefficient, typically 10^5 times the molecular viscosity ν in the atmosphere. From the right-hand side, we see *turbulent* kinetic energy is always *generated* by shear from the energy of the basic flow (first term), by buoyancy (second term) if positively correlated, as before, and *lost* by dissipation, third term. *Div* on the left-hand side means divergence of several flux terms, like that of turbulent kinetic energy $\overline{e}$ with the mean flow $\frac{\partial}{\partial x_j}\overline{v_j e}$. This equation is valid neither locally nor instantaneously. To make use of it, one has to employ averaging, either along homogeneous spatial dimensions, over time in stationary conditions, ensemble averaging over several realisations, or a combination [9]. Through this averaging procedure, all thermals are gone, only something similar to the ensemble average of their effects is left [8]. So, we use the total kinetic energy equation for analysis.

Simplified model cases are calculated using Large Eddy Simulation (LES), utilizing the PALM program system of the Institute of Meteorology and Climatology at Leibniz Universität Hannover [10]. In LES each physical variable consists of three components, e.g. for potential temperature $\theta = \overline{\theta} + \theta' + \theta''$, the final summand θ'' being the sub-grid scale (SGS) contribution, which is parameterized and (with the exception of e'') not a direct calculation result, as opposed to the resolved scale $\theta^* = \overline{\theta} + \theta'$, marked with an asterisk. However, for some physical variables the order of magnitude of their averaged SGS can be calculated statistically and compared to their resolved scale averages.

To better understand the origin and development of thermals, calculation results are analyzed with respect to the budget equation for total specific kinetic energy.

Horizontally homogeneous static case

First calculations aim to identify the mechanism of free atmospheric convection, with boundary conditions as simple as possible: a stationary, horizontally homogeneous situation, but without mean flow (so all flow is turbulence!) and without humidity, heated from the ground, and with a grid as fine as possible for the capacities of the personal computer (PC) employed. In addition to the standard PALM output, the terms of the instantaneous kinetic energy budget are calculated by user-code.

- Calculation domain, see Fig. 1: $2{,}000^3$ m³ with parent grid resolution of $12\times12\times12$ m³, and a nested child grid from the ground up to 200 m with a $6\times6\times6$ m³ resolution, alternatively, to check convergence, $3\times3\times3$ m³ up to 100 m. Lateral boundary conditions are cyclical. A ground-level Monin-Obukhov similarity theory layer is used to introduce boundary conditions into the atmospheric model, here turbulence is fully parameterised. Rayleigh damping in the model region well above the inversion is used to avoid gravity wave artefacts. At the simulation start, turbulence is triggered by imposing random, small velocity fluctuations.

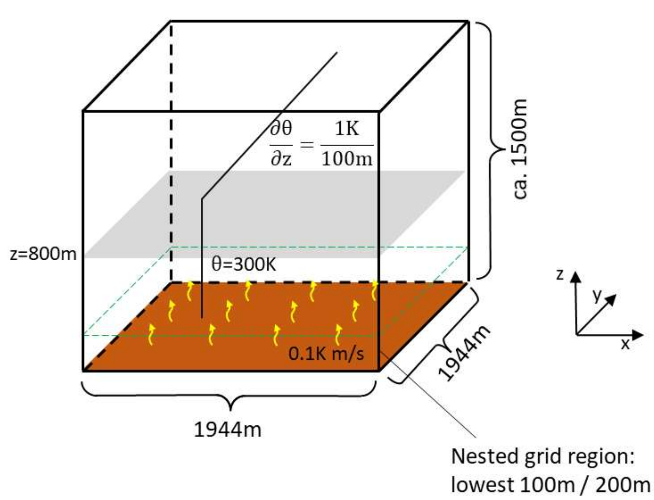

Fig. 1: Model set up. Adapted from [11].

- Initial condition: well-mixed boundary layer with constant potential temperature up to an inversion, initially at 800 m, above which potential temperature increases at a constant rate of 1 K/100 m. Surface heat flux is 0.1 Km/s, about 120 W/m².

Time series data (Fig. 2) of kinetic energy and of maximum vertical velocity show, that after two hours the spin-up is completed and a quasi-stationary state is achieved. As a sanity check, height profiles of resolved scale and subscale energy fluxes are compared in Fig. 3. The top diagram shows the mixed layer parent grid data up to the inversion, which has risen from the initial 800 m to about 1,050 m. The lower part of top diagram with higher vertical resolution shows data from the child data set. LES results are reliable, if resolved scale flux is significantly larger than sub-grid scale energy flux. With 6^3 m^3 nested grid resolution this happens at 12 m height and above. Fig. 3 bottom shows the same information for 3^3 m^3 nested grid resolution. Resolved scale flux dominates sub-grid scale flux at 6 m and above (nested grid). However, the interpolation to the parent grid overshoots at 12 m and undershoots at 24 m, due to the highly nonlinear characteristics in the constant flux layer, see region marked by red ellipse. We take the nested grid data where available.

Figure 4, generated from the 3D data sets with the NASA earth data analysis tool Panoply [12], compares results of potential temperature calculations with the 6^3 m^3 nested grid (top two diagrams), left from the parent grid, right from the child grid, and 3^3 m^3 nested child grid (bottom). All diagrams show a pattern with relatively cold cells occupying a major share of the area, relatively narrow warmer edges and warmest small spots at knots of several meeting edges. The cell size is identical in all

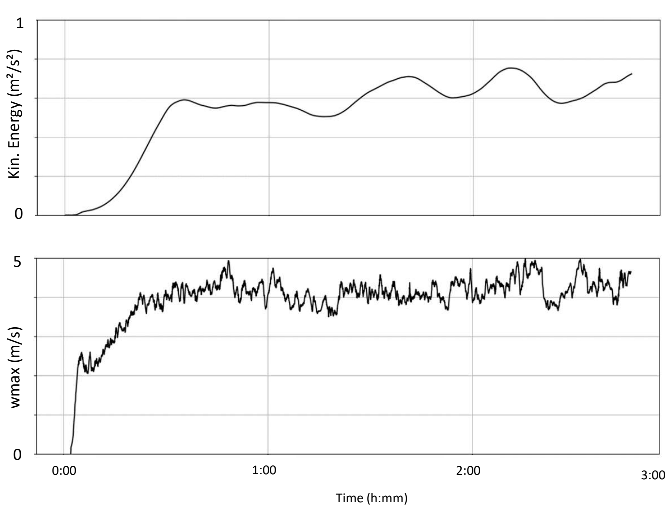

Fig. 2: Time series of specific kinetic energy (top) and maximum vertical velocity *wmax* (bottom) at 6^3 m^3 nested grid resolution.

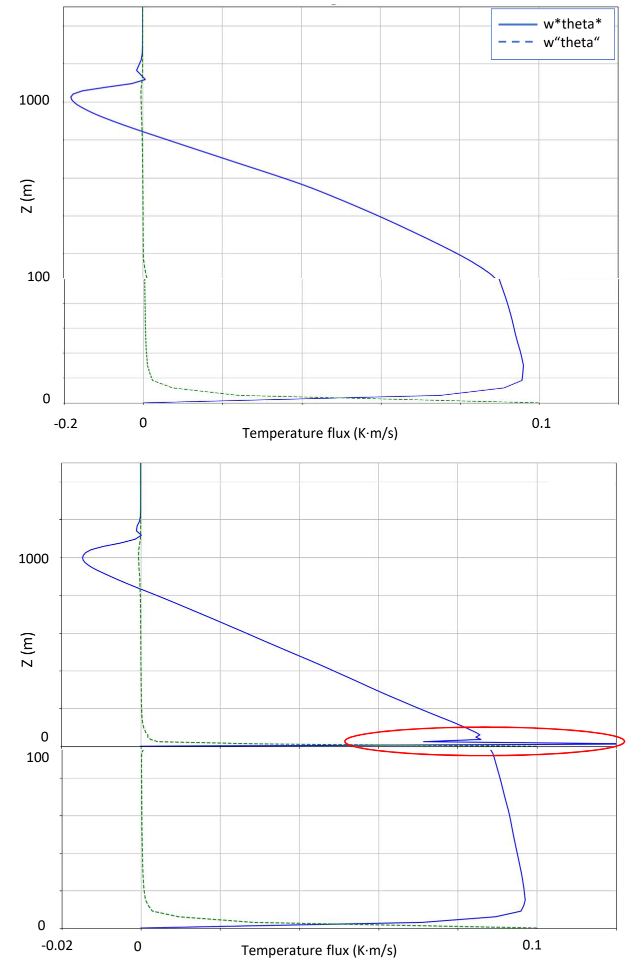

Fig. 3: Top: Comparison of resolved and subscale temperature flux at 6^3m^3 nested grid resolution. Lowest 100 m is an enlarged vertical scale, child grid data near the surface.
Bottom: Comparison of resolved and subscale temperature flux at 3^3m^3 nested grid resolution. The red ellipse highlights an artifact resulting from grid nesting in parent grid data.

diagrams, indicating that the flow structure is captured correctly already with 6 m resolution. The child grid top right picture is a "sharpened" version of the top left interpolated version. Furthermore, a significant area is colder than 301 K, the lower scale limit, and is coloured dark blue. The maximum temperatures are identical at 302.9 K.

The 3^3 m^3 nested child grid (bottom picture) does not show an identical pattern. Due to the random triggering, further build up too is basically stochastic, but results in a pattern of the same "topology". It is even "sharper", with steeper gradients and slightly lower minimum temperature, but significantly higher maximum temperature 303.7 K. Giersch and Raasch [11] found that these steeper gradients and higher maxima continue to get steeper and higher down to grid resolutions of 0.625^3 m^3, probably the finest resolution computed so far.

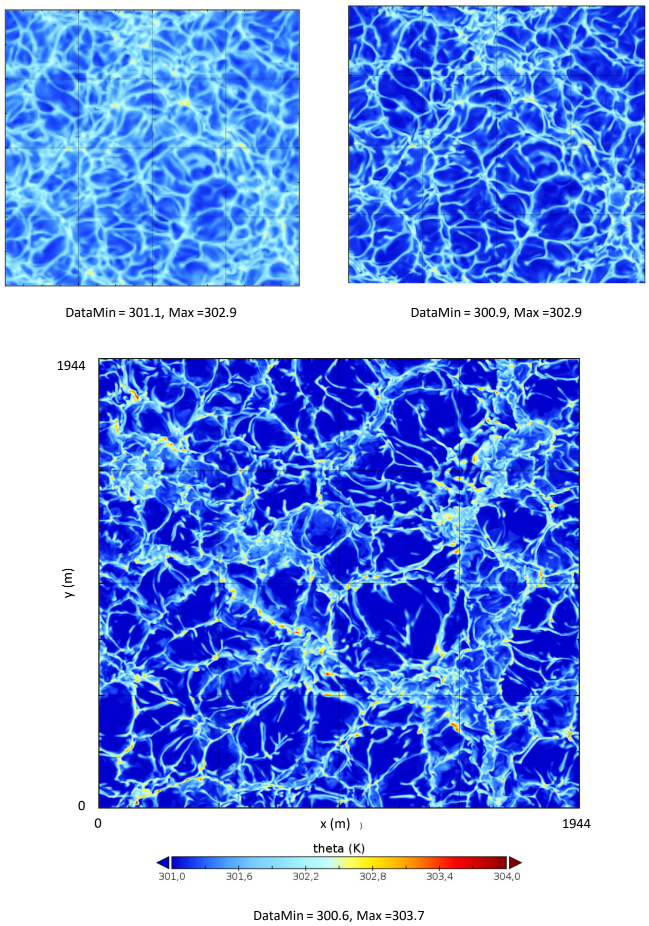

Fig. 4: Potential temperature horizontal *xy*-sections near the ground, identical physics but different calculations are compared. Top two diagrams at 6 m from nested grid 6^3 m^3 calculation, left parent grid 3D data, right the nested grid data. Bottom diagram at 9 m from nested grid 3^3m^3 calculation. All scales as in bottom diagram.

Figure 5 shows the temperature distribution varying over height, top from the parent data, bottom from the child data. The distribution is very asymmetrical, with the maximum difference between the 10th percentile and the median being 0.1 K only, and over most of the mixed layer height well below 0.05 K, but the 90th percentile being more than 0.3 K and up to 1 K warmer than the median in the lowest third of the mixed layer.

With VAPOR [13, 14] it is possible to generate impressive 3D movies of the flow. Fig. 6 shows a raytracing image of all volume being 0.5 K and above warmer than the respective horizontal mean, coloured red, or 0.3 K and below cooler, coloured blue. The picture is slowly moving and fluctuating over time, but the principal pattern of cells with its structure size does not change.

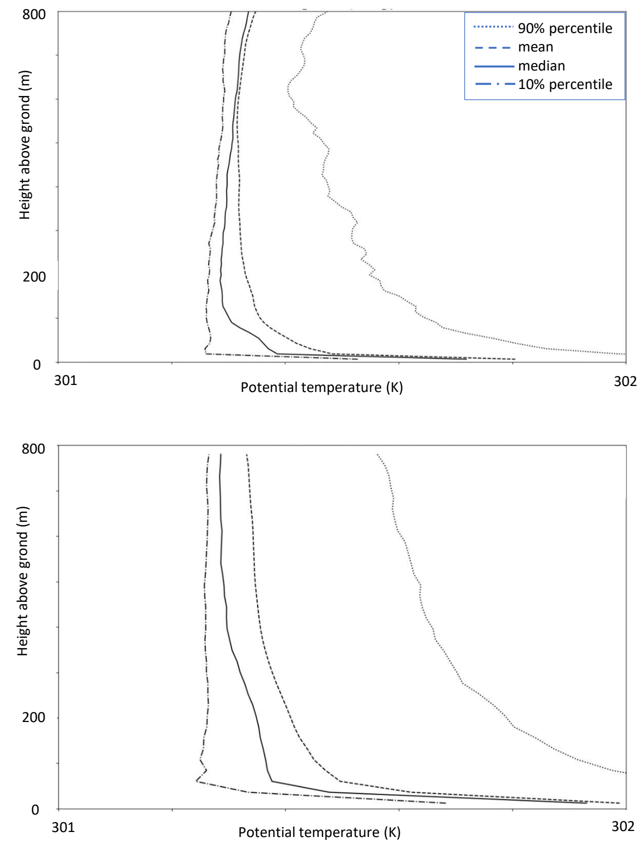

Fig. 5: Temperature distribution over height above ground, parent grid (top) and nested 6^3m^3 child grid (bottom).

Figure 7 shows path lines, the 5-minute history of 1,000 particles, starting from the surface up to 300 m above the surface. The initial positions are chosen randomly, but the more probable, the higher their pt_flux (buoyancy excess).

- There is one structure with high kinetic energy, its vertical orientation indicating that mainly vertical velocity contributes to its kinetic energy, and a lot of “disrupted” structures with lower energy.
- Quite a few parcels achieve 4 m²/s² kinetic energy within 300 s.
- Many parcels do not rise despite their initial advantage, and achieve less than 1 m²/s² specific kinetic energy.

Unfortunately, VAPOR does not have the option to integrate path lines backwards in time to investigate the root cause of one or the other development. But the path line data can be exported and evaluated further in Excel. Fig. 8 shows the specific kinetic energy development of the ten highest energy path lines, taken from two different clusters:

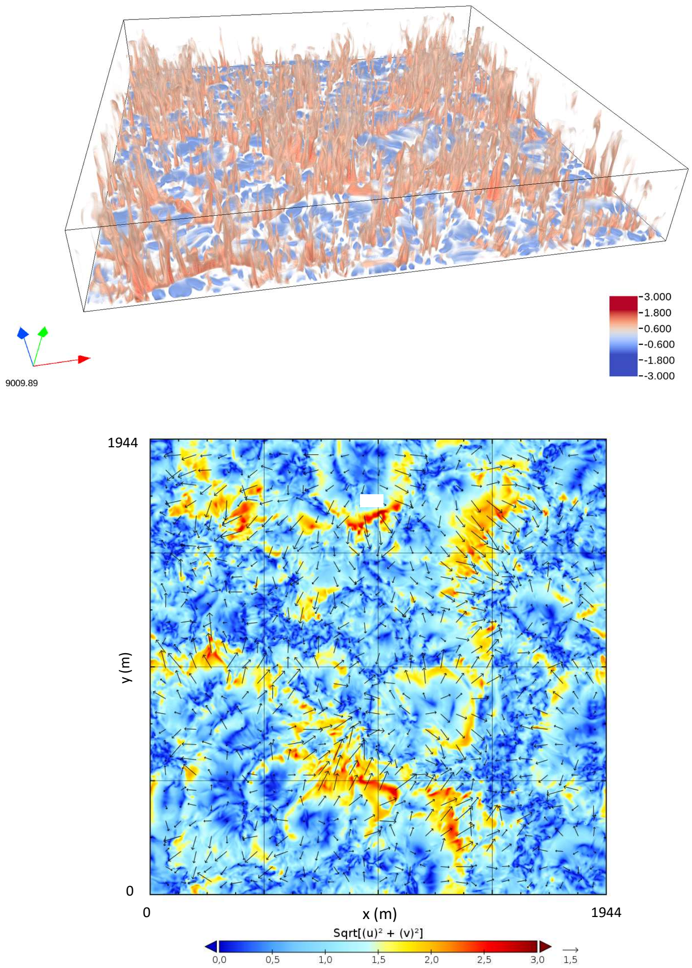

Fig. 6: Top: 3D view of lowest 100 m AGL excess temperature d_{pt}. Vertical scale 3 times horizontal scale.
Bottom: horizontal xy section 9m above ground, velocity direction (arrows) and magnitude (colour scale) flow pattern.

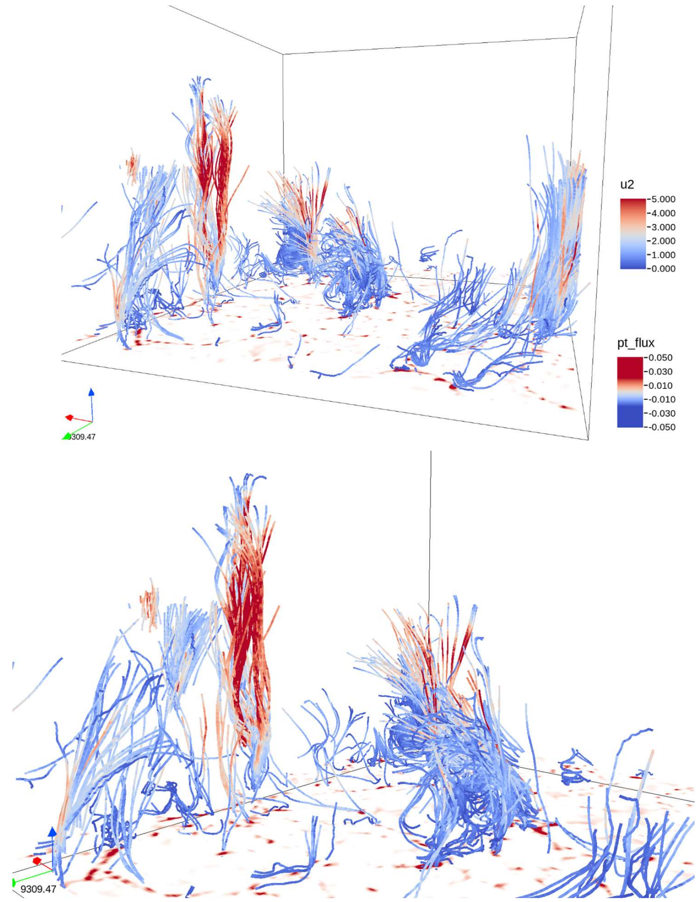

Fig. 7: 300 s Path lines starting from below 300 m above the surface, distributed randomly but with a bias of maximum buoyancy (Top image), and enlarged view of strongest thermal (Bottom). Coloured with their instantaneous kinetic energy $u2$. Surface area with slice image of buoyancy pt_{flux}.

- Even the largest energy thermals develop with constantly large rate of about 0.05 m²/s³ for only some seconds, always followed by periods of constant or even decreasing energy.
- Overall, the average increase rate is about 0.02 m²/s³. So, it takes several minutes for a 3 m/s thermal to develop. Energy loss is similarly slow.
- Neither instantly nor averaged over 60 s, there is a strong correlation between resolved scale change rate of specific kinetic energy and resolved scale pt_flux buoyancy plus vnap pressure fluctuation advection (not shown in picture). The orders of magnitude are matching, verifying the analysis approach. The diffusive term as well as dissipation calculated from the resolved scale data are very small, but their sub-grid-scale contributions are significant, as shown e.g. by Heinze et al. [9]. Their calculation would require averaging both horizontally and over much longer time, but this paper looks for local and instantaneous effects.

Next, we examine vertical sections in the *xz*-plane, chosen in time and *y*-position to incorporate a strong thermal. Figure 9 is a synopsis of several physical parameters of the same section at $y = 450$ m through the flow field, averaged over 60 s. Why 60 s averaging time? 60 s is about the time a glider pilot in search for a thermal needs to complete a shallow circle, and therefore is the analysis time step to compare flow features. The top two images show again the strong correlation of total specific kinetic energy $u2$ and vertical velocity w. The middle row shows buoyancy and advection of pressure gradient, one time step and 60 s earlier, the contributors to the build-up of specific kinetic energy. The bottom row shows a flow field detail and the magnitude of curl of the velocity field, called turbulence intensity ti. There is a strong thermal at $x = 1{,}700$ m (circled), with large energy and vertical speed from 400 m above the surface to the inversion at 1,000 m. It is constructed by a region of upwards buoyancy pt_flux reaching from the ground up to 700 m. Pressure advection (vnap) contributes in the same order of magnitude, locally positive, locally negative thus in total probably neutral. Remarkable is the relatively small turbulence intensity ti in the core of the thermal, but large ti at its "skin" with larger shear.

In Fig. 9 at x = 350 m there is another region of high buoyancy near the ground (circled), but it collects neither significant kinetic energy nor vertical velocity in the following time steps. Buoyancy support pt_flux from the ground is similar to the strong thermal, and below 100 m there is even support by pressure advection (vnap). But from 100 m to 200 m there is strong negative pressure advection, killing the thermal. The flow field detail shows a collision with a wide and quite strong downdraft from above (circled "failing thermal"), and apparently deflecting flow and its energy to the right, to the major thermal at x = 1,700 m. Turbulence intensity has a local maximum in the collision region.

Topography

The next topic is the influence of topography. A pyramid shaped hill was designed, as illustrated in Fig.10, so that solar irradiation at noon of June 21st at 53°N is perpendicular to the southern slope resulting in an insolation of about 1000W/m². On the northern slope insolation is less than half the value of the southern slope. On the eastern and western slopes and on the flat ground the insolation is about 13% less. The parent grid has 12^3 m³ resolution. The child grid with 6^3 m³ resolution up to nearly 600 m includes the hill and above. Initially, the inversion is at 1,200 m above flat ground. Again, the lateral boundary conditions are cyclical, effectively repeating the single hill infinitely both in North-South and East-West directions.

Figure 10 bottom shows the flow field in a North-South vertical section through the top of the hill, with a combination of child grid data below 600 m, and parent grid data above. There is terrain-following anabatic uphill flow along the southern slope, and strong updrafts above. Inertia of the northerly flow along the surface can move updrafts beyond the top, but generally (in this section) the air is sinking above the Northern slope, and the adjacent flatland.

Figure 11 top shows velocities in a terrain following section at 12 m above the surface, with southerly and westerly uphill flow on the southern and western slopes. Figure 11 bottom shows the temperature distribution in the same terrain following section, resulting both from uneven insolation as well as from the flow pattern. The temperature again has the well-known cellular pattern, being warmer on the south and west slope up to the summit. The north slope is less irradiated and significantly cooler. The differences of maximum and minimum temperature are located too above the south and west slopes, amounting nearly 5K, significantly larger than above flat terrain, where it was 2K. So the glider pilot will find more likely a thermal above the south and west slopes.

Humidity and horizontally inhomogeneous cases in the course of the day

Incorporating the influence of humidity into the calculation requires solving an additional transport equation and defining appropriate initial and boundary conditions for the mixing ratio q, which is treated as a conserved scalar. In the absence of phase changes — such as evaporation or condensation — the only change in the differential equation is to substitute all occurrences of the potential temperature, variables $\overline{\theta}$ and θ', with their virtual potential temperature counterparts θ_v, with

$$\theta_v = \theta\,(1 + 0.61q)\,. \tag{6}$$

As both θ and q are influenced by the same processes (advection, turbulent mixture) over most of the boundary layer, humidity should not change anything there. Boundary and initial conditions may make a difference. At the surface there is evaporation and a latent heat flux, typically in the same direction as the sensible heat flux, requiring quite a large share of the net radiation, and thereby reducing the sensible heat flux. The result is less buoyancy than without humidity. The free atmosphere air above the inversion typically is drier than the boundary layer (besides being warmer). By the turbulent thermal air penetrating into the laminar free atmosphere some free atmospheric air is captured, and mixed downwards into the boundary layer, a process called entrainment. Thus, on average the top of the boundary layer will be warmed from above, reducing buoyancy of thermals, but also dried, which has an increasing effect on buoyancy up there. Maas and Etling [5] concluded that "humidity effects do not lead to stronger thermals but rather lead to colder thermals, for a given surface buoyancy flux".

As suggested by [5], our further calculations include the effects of:

- Daily variation of solar irradiation with a clear sky model and a balance of surface energy, over 60 h model time - see Fig. 12 top.
- Explicit humidity calculation, but condensation of water vapor is avoided by appropriate setup of atmospheric humidity, i.e. limitation to blue thermal conditions.
- Soil model with heat conduction, water diffusion and water transport through vegetation, to evaluate sensible and latent heat flow into the atmosphere.
- Flat terrain structured with three surface types, including areas of water, vegetation, and asphalt, as shown in Fig. 12. The red square delineates the model region, with surface types coded as follows: grey represents asphalt, green denotes low grass on medium-fine soil, and blue indicates water. The surface type pattern is repeated outside of the model domain as cyclical lateral boundary conditions.
- Superimposed wind.

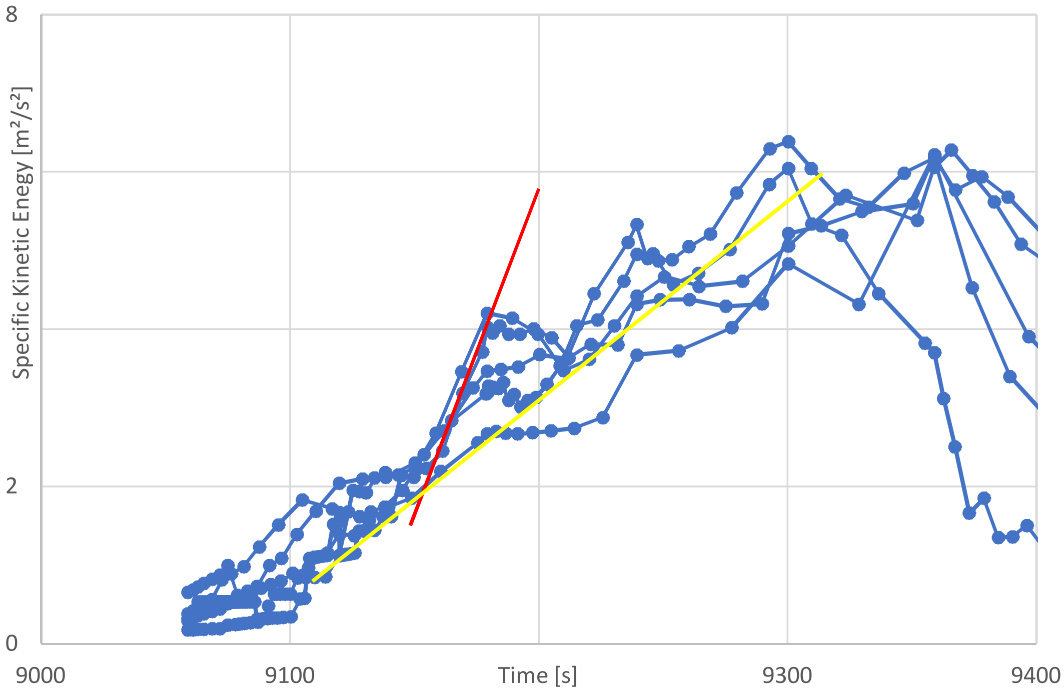

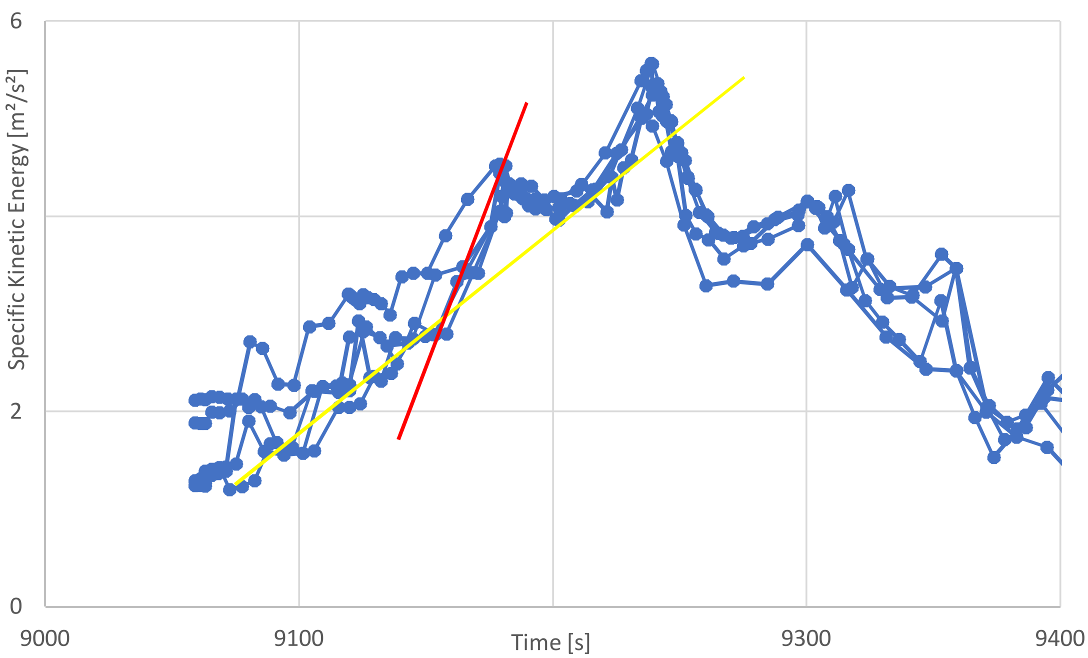

Fig. 8: Specific kinetic energy of ten highest energy path lines over time, taken from two different thermals. Yellow lines indicate average vertical acceleration, red lines maximum acceleration.

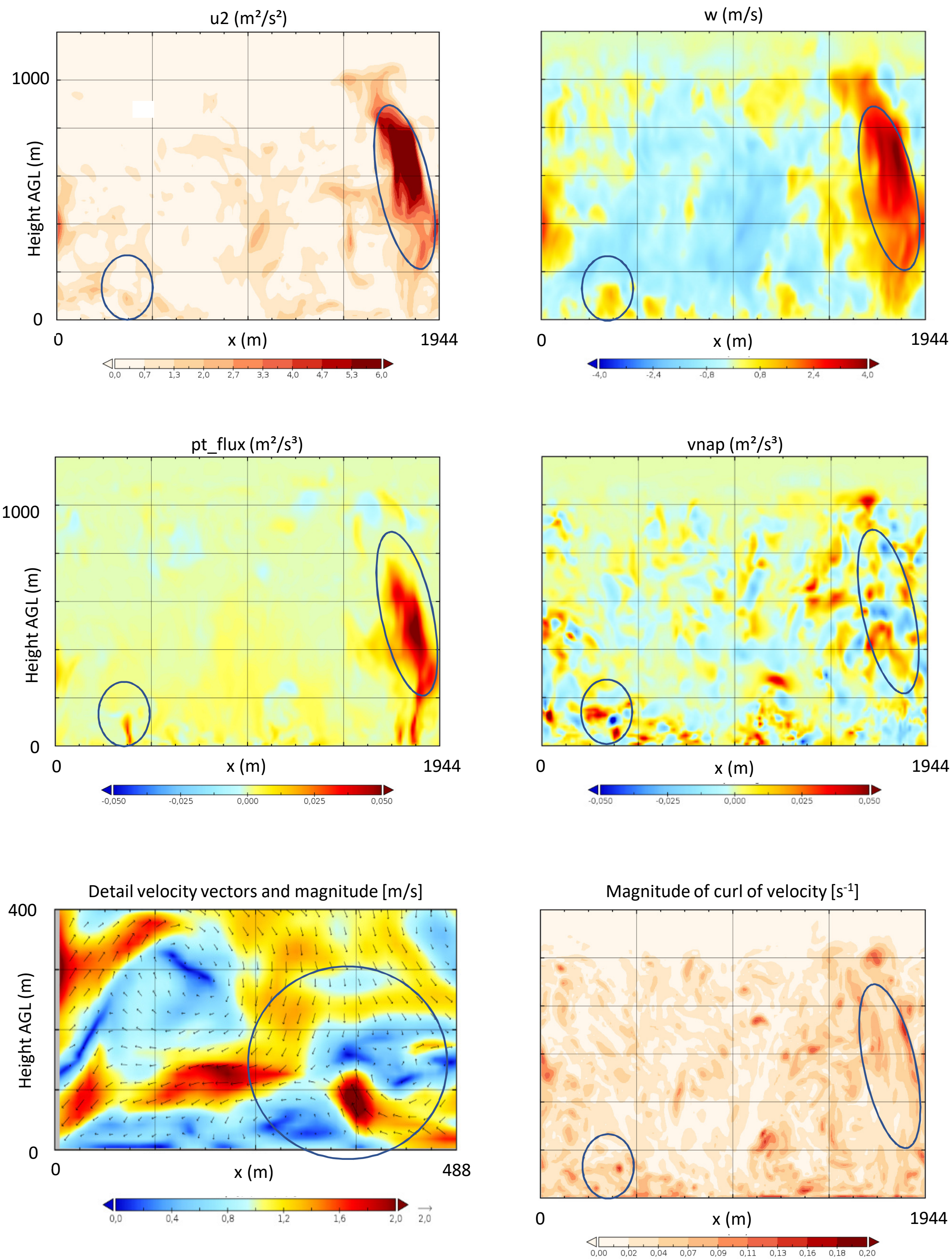

Fig. 9: Vertical sections through 60 s averaged 3D data at y = 450 m. Top row: specific kinetic energy and vertical speed; middle row: buoyancy and pressure gradient advection one timestep or 60 s before; bottom row: flow field detail of "failing" thermal and magnitude of curl of velocity, i.e. turbulence intensity.

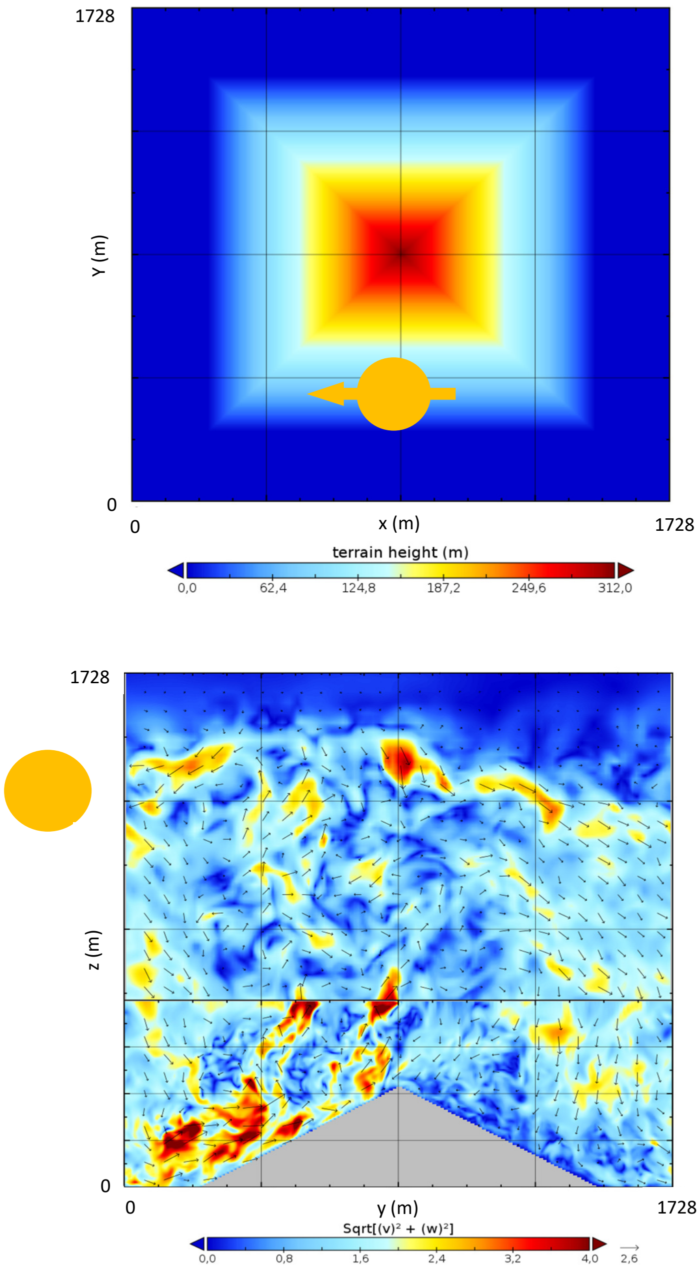

Fig. 10: Thermal formation over a hill, with the initial inversion at a height of 1200 m. Orange circles and arrow indicate current position and further movement of the sun at about noon. Top: Pyramid shaped hill geometry. Bottom: vertical flow field in N-S section through peak; data in the lowest 600 m are from child grid, above from parent grid.

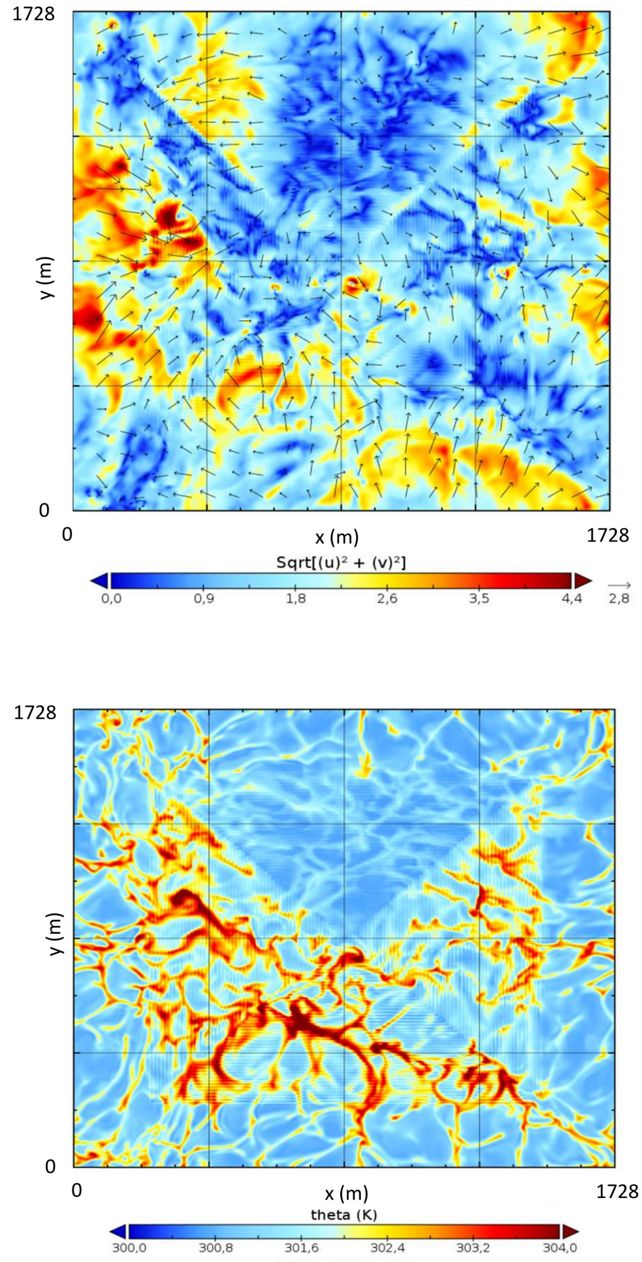

Fig. 11: Top: horizontal flow field 12 m above ground, following terrain. Bottom: instantaneous temperature 12 m above ground.

- Grid size typically 2000×2000×2500 m³ with a resolution of 50×50×25 m.

Figure 13 shows the surface energy budget after 48 h, at noon local time on the third day. The top left is the net radiation budget, which results from different albedo and surface temperature values. As water is modeled with zero albedo and has the lowest surface temperature at noon, it gets the highest net radiative power of about 870 W/m². Asphalt and grass show a similar net radiative power of about 500 W/m², but asphalt has a lower albedo with a higher surface temperature. Ground heat flux is a minor factor of 50 to 100 W/m² for grass and asphalt. Water not only absorbs all radiative power, it also has a negative sensible

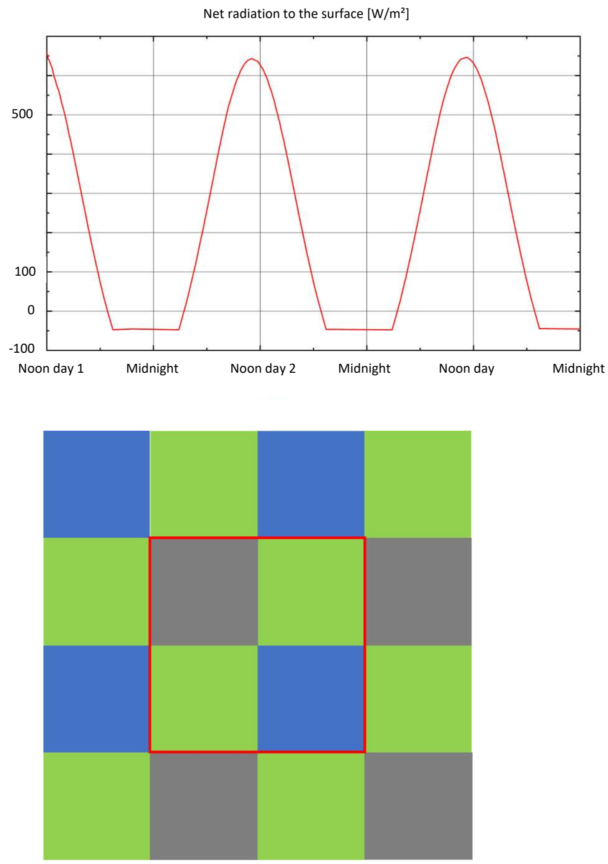

Fig. 12: Top: net radiation budget over time. Bottom: surface structure - grey is asphalt, green is fine soil with grass vegetation, blue is water. The red square outlines the computational domain.

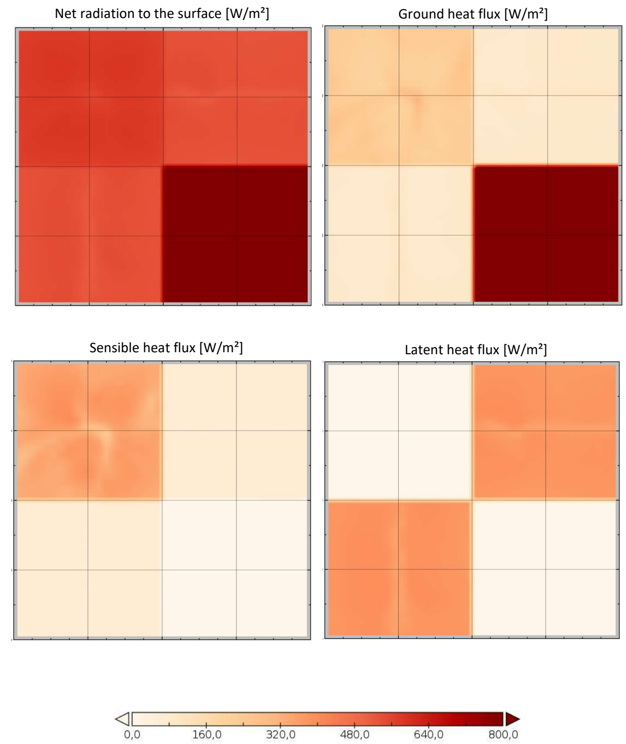

Fig. 13: Surface energy budget at 1200 loc. Top: net radiation budget and ground heat flux; bottom: sensible heat flux and latent heat flux.

heat flux (SHF), as at noon the air is warmer than water (water is modeled with constant temperature due to its high heat capacity). Asphalt has the largest SHF value at about 400 W/m², but a latent heat flux (LHF) of zero, as there is no water to evaporate. For the grass surface, the LHF is about 300 W/m² and the SHF about 100 W/m².

Figure 14 looks into the soil below the surface, at positions indicated by crosses in the right column. Top picture shows humidity below the grass surface, decreasing slowly during the days, but only in the uppermost few cm of the soil. The middle picture shows soil temperature below the grass surface, with heating during days, and cooling during nights. The maximum soil temperature in the afternoon of the third day is about 303K, 10K warmer than initially. Asphalt effectively seals humidity in the soil below, which hence does not cool through evaporation. This has a tremendous effect on soil temperature, as shown in the lowest picture - the soil temperature rises to 329K in the afternoon of the third day.

This causes a convective cell structure, Fig. 15, with an extremely strong updraft above the asphalt, centre at x = 600 m, top picture. The maximum vertical velocity seems to be limited to a tube of 100 m radius, and a height between 400 m and 1,300 m, penetrating far into the inversion. Also, there is upward motion above the grass, $x>1{,}000$ m, but limited to z = 500 m, and significantly slower, $w<2$ m/s. Above z = 500 m, all upward motion is sucked into the asphalt thermal. The flow pattern above the grass, shown in the second section, with changed velocity scale, shows horizontal flow towards grass centreline at x = 500 m, and rising there with up to 2 m/s and z = 400 m, from the water areas, $x<0$ and $x>1{,}000$ m. In the bottom there is a horizontal section of horizontal flow at z = 37.5 m, showing flow to grass field centre lines, into asphalt centre point, and low velocity above water.

What happens over time? Figure 16 shows virtual potential temperature and mixing ratio above the asphalt surface. Virtual potential temperature, top picture, rises with time, from left to right, quite uniformly through the boundary layer. The capping inversion rises through the days. During the nights a surface inversion develops below z = 100 m. Mixing ratio, bottom, also increases from left to right. The increase continues also during the nights, but is then capped by the surface inversion. When the surface inversion is broken in the morning for the first time, the thermal carries more humidity, but this high concentration is mixed into the whole boundary layer within a short time. Furthermore, the thermal is located above the highest surface sensible heat flux, neither above water nor above grass, so even in this moment humidity is not the dominating force [3], but the stowaway.

Figure 17 shows a probably more realistic scenario, with reduced asphalt and water surface fraction, but more grass. The strong thermal is still above the asphalt surface, top picture, but with reduced vertical top speed and reduced diameter. It is strongest in the uppermost region, after joining of two separate thermals from below. The thermal over grass, bottom, is slightly stronger and reaches slightly higher than in the former scenario.

Figure 18 illustrates the effect of a modest wind of 2.5 m/s in x direction. Wind seems to separate the thermal columns into bubbles and takes them with it. The strongest updraft is not directly above the asphalt anymore, but in lee of it, as seen in the top picture. The bottom picture shows an updraft over the water surface, but there is mainly horizontal speed and little updraft, as indicated by the wind arrow direction.

The mean wind in the convective boundary layer is almost homogeneous, parallel to the geostrophic wind over flat land, and nearly constantly strong at 200 m and above. If we subtract the mean wind profile from the flow field, we see that the thermal bubbles, as indicated by the velocity vectors in them, are oriented nearly vertical and drift with the mean wind, Fig. 19.

Very interesting is the comparison between grass vegetation and forest vegetation, by just replacing the grass by forest, leaving everything else unchanged. The virtual potential temperature flux, the inversion height and the variance of vertical velocity w are much higher in a "forest scenario", Fig. 20. Looking into the parameterisation, forest has a higher "leaf area index" compared to grass, which should promote evaporation over heating. But forest has much a higher surface friction than grass, causing a lower velocity gradient in the surface layer, Fig. 21 top. So, evaporation is reduced over forest, Fig. 21 bottom, and thermal strength is improved!

Conclusions

Most of the conclusions may not be new to meteorologists. For many glider pilots they may be interesting and hopefully are helpful to succeed in blue thermal conditions!

- In the lowest part of the convective boundary layer some air is significantly warmer than the average, less dense, and is accelerated upwards, thereby exchanging internal energy into "vertical" kinetic energy. Vertical acceleration needs horizontal deceleration and convergence, because of continuity, making warm air concentrate.
- If not disturbed, further kinetic energy builds up through buoyancy flux, the product of vertical velocity and potential temperature excess, even above half of the inversion altitude, where hardly any potential temperature excess is measurable anymore. Moisture is not needed anymore to explain this fact.
- There is no continuous acceleration, even the highest energy thermals are disturbed multiple times in their history. The strongest thermals build from the joining of smaller thermals.
- At the top of the convective boundary layer, thermals penetrate into the inversion - the higher their energy, the deeper. Through entrainment there is heating, and continuity makes warm air sink. The negative buoyancy flux has a leveling effect on the kinetic energy of sinking air, the fastest parcels decelerate most. Most of the air of the convective boundary layer is a little cooler than the horizontal average and sinking slowly.
- In homogeneous, blue conditions strong lift can be anywhere, is invisible and quite rare.
- Differences of the surface character and topography organize the thermal convection into cells and determine where updrafts are located. The strongest thermals are above asphalt surfaces, where evaporation is inhibited, and all radiative flux is used for heating of the ground and the atmosphere. Heating and thermals are stronger above forest than above grass.
- To find thermals as a glider pilot, follow the rules of Helmut Reichmann [15]: Imagine to walk barefooted and feel the highest temperatures!

Acknowledgments

I am indebted to Siegfried Raasch for developing and providing the PALM software, and teaching its proper use to the students like me!

I thank two reviewers of this paper for challenging me to improve it, and their kind advice!

References

[1] Carsten Lindemann. Some characteristics of thermal convection. In *Proceedings XV OSTIV CONGRESS*, Räyskälä, Finland, 1976. URL: `https://journals.sfu.ca/ts/index.php/op/article/view/1818/1739`.

[2] Albert Kiessling. Measurement results from warm air thermals over the namibian steppe. In *Proceedings XXXIV OSTIV CONGRESS*, pages 126–129, Hosín, Czech Republic, 2018. URL: `https://ostiv.org/congress/congress-events/congress-details/xxxiv-congress.html`.

[3] Oliver Predelli and Ronald Niederhagen. Humidity, the dominating force of thermal updrafts. *Technical Soaring*, 45(1), 2021. URL: `https://journals.sfu.ca/ts/index.php/ts/issue/view/231`.

[4] Ines Schäfer, Daniel Hardt, and Kai Rohde-Brandenburger. Feuchtemessung mit Flugzeugen - Stand der Technik. In *Vortrag auf dem 46sten Segelflugsymposium*, Braunschweig, 2022. contact author for this document.

[5] Oliver Maas and Dieter Etling. On the influence of moisture on the strength of thermals: A large-eddy simulation case study. *Technical Soaring*, 45(3), 2021. URL: https://journals.sfu.ca/ts/index.php/ts/issue/view/235.

[6] Dieter Etling. *Theoretische Meteorologie: Eine Einführung*. Springer Berlin Heidelberg New York, 2008.

[7] John C. Wyngaard. *Turbulence in the Atmosphere*. Cambridge University Press, Cambridge, UK, 2010.

[8] Siegfried Raasch. Lecture notes on atmospheric convection, 2021. contact author for this document.

[9] Rieke Heinze, Dmitrii Mironov, and Siegfried Raasch. Second-moment budgets in cloud topped boundary layers: A large-eddy simulation study. *J. Adv. Model. Earth Syst.*, 7:510–536, 2015. doi:10.1002/2014MS000376.

[10] Björn Maronga et al. Overview of the palm model system 6.0. *Geoscientific Model Development*, 13:1335–1372, 2020. URL: https://gmd.copernicus.org/articles/13/1335/2020/, doi:10.5194/gmd-13-1335-2020.

[11] Sebastian Giersch and Siegfried Raasch. How do dust devil-like vortices depend on model resolution? a grid convergence study using large-eddy simulation. *Boundary-Layer Meteorology*, 187:703–742, 2023. doi:10.1007/s10546-023-00792-3.

[12] Panoply: A nasa visualization tool. URL: https://www.giss.nasa.gov/tools/panoply/.

[13] S. Li, S. Jaroszynski, S. Pearse, L. Orf, and J. Clyne. VAPOR: A visualization package tailored to analyze simulation data in earth system science. *Atmosphere*, 10(9):488, 2019. doi:10.3390/atmos10090488.

[14] Visualization & Analysis Systems Technologies. Visualization and analysis platform for ocean, atmosphere, and solar researchers (VAPOR version 3.8.0) [software], 2023. doi:10.5281/zenodo.6567350.

[15] Helmut Reichmann. *Streckensegelflug*. Motorbuch, Stuttgart, 1989.

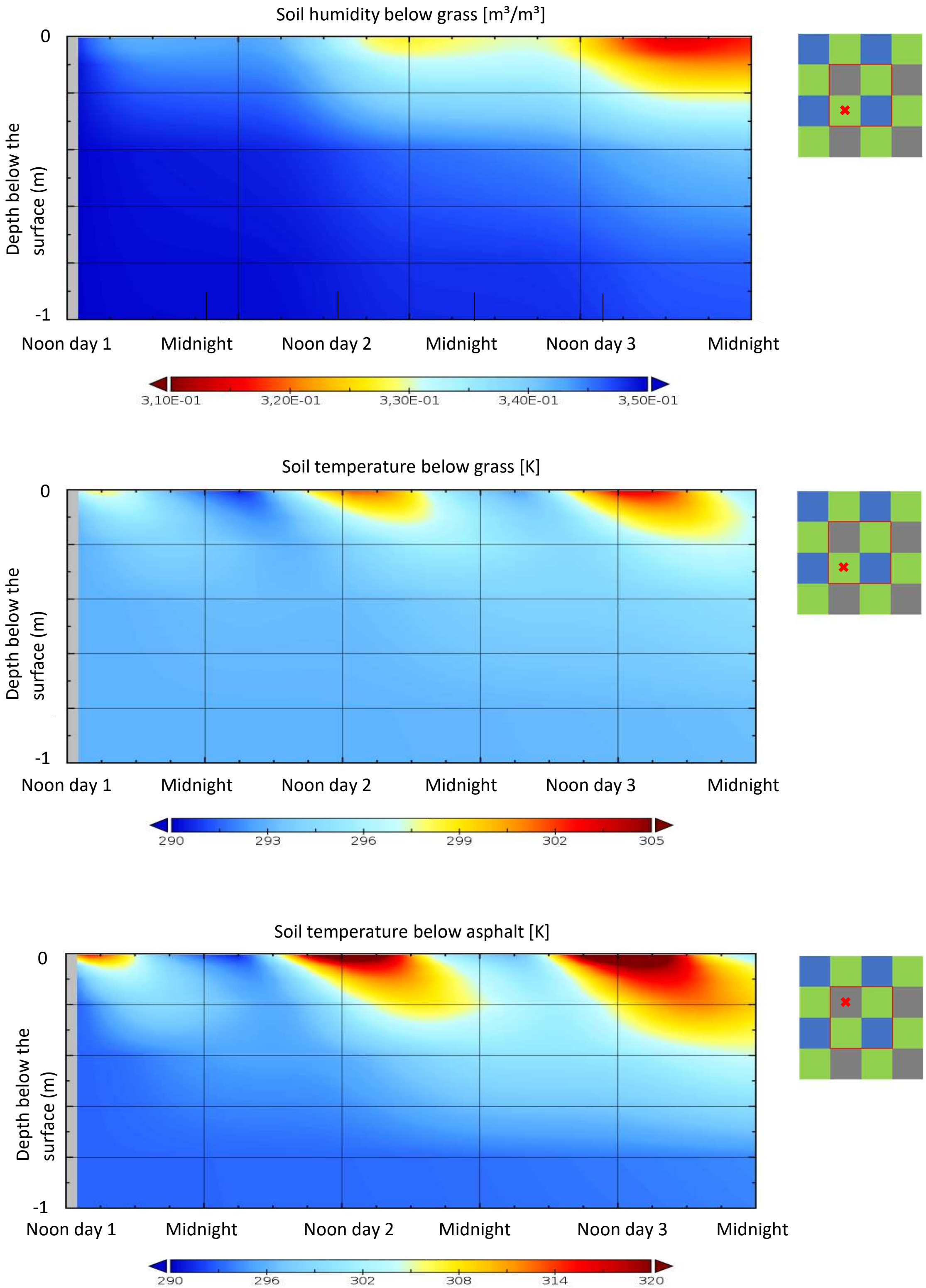

Fig. 14: Top: soil humidity below grass vegetation. Middle: soil temperature below grass. Bottom: soil temperature below asphalt surface, enlarged scale here.

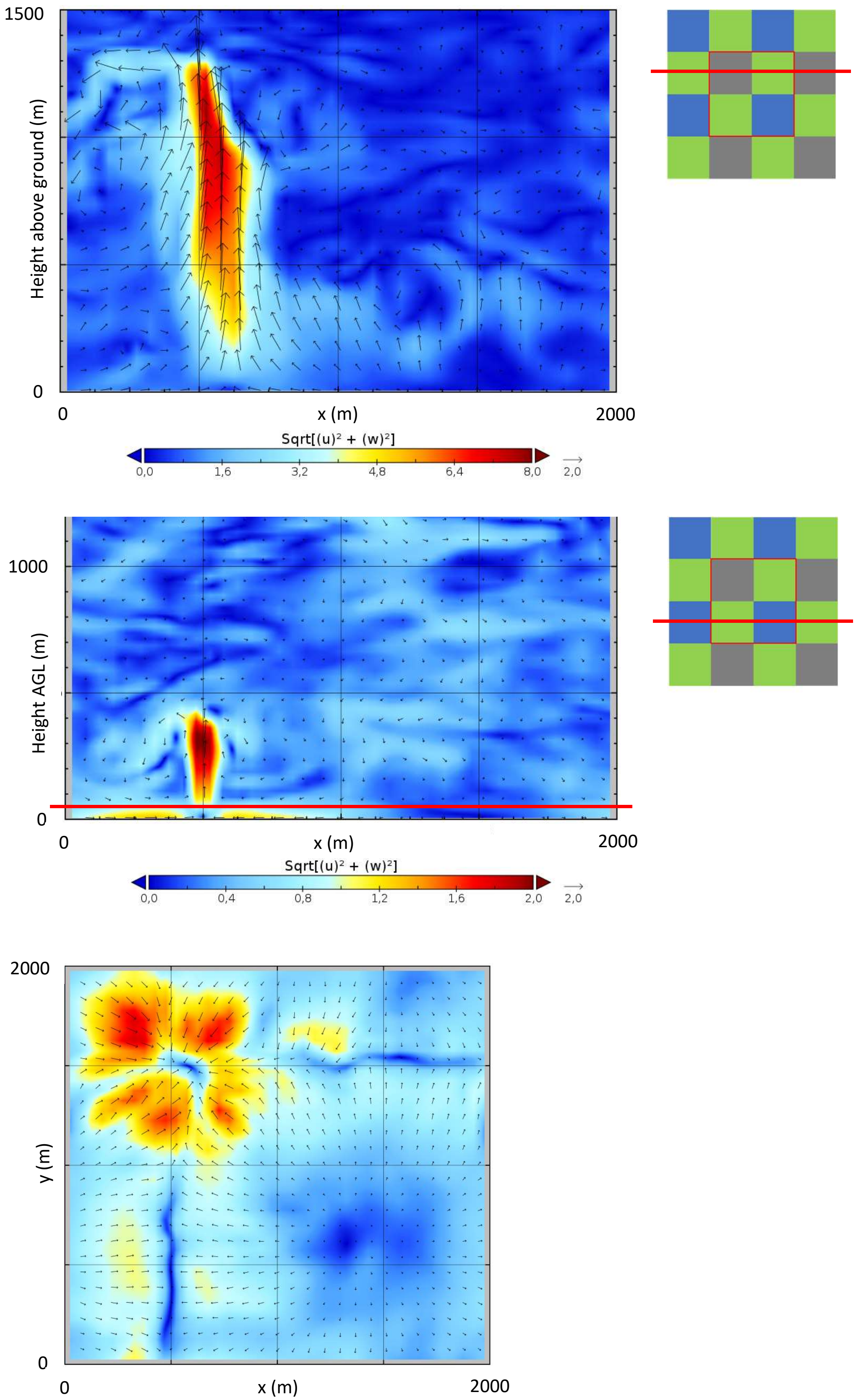

Fig. 15: Flow pattern after 48 h. Top: vertical velocity field [m/s] in section through asphalt and grass. Middle: vertical velocity field, section through grass and water, scale reduced. Bottom: horizontal velocity field at 37.5 m height, same velocity scale as the middle diagram.

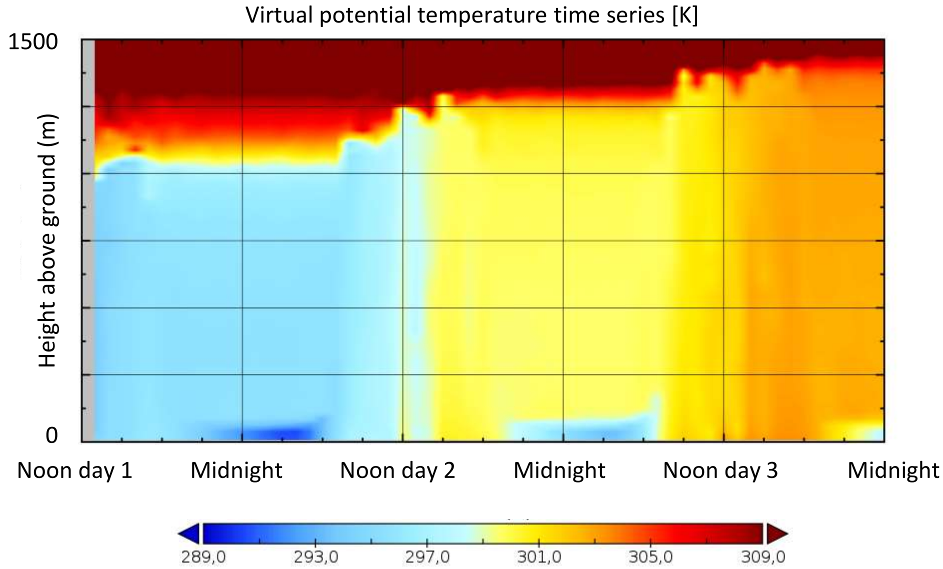

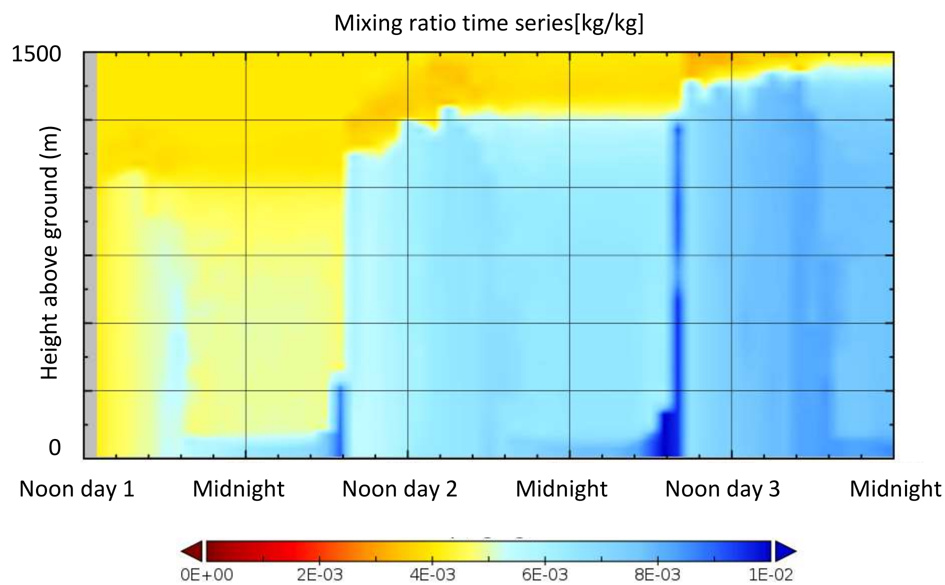

Fig. 16: Virtual potential temperature and water vapor mixing ratio over time, both above the asphalt surface.

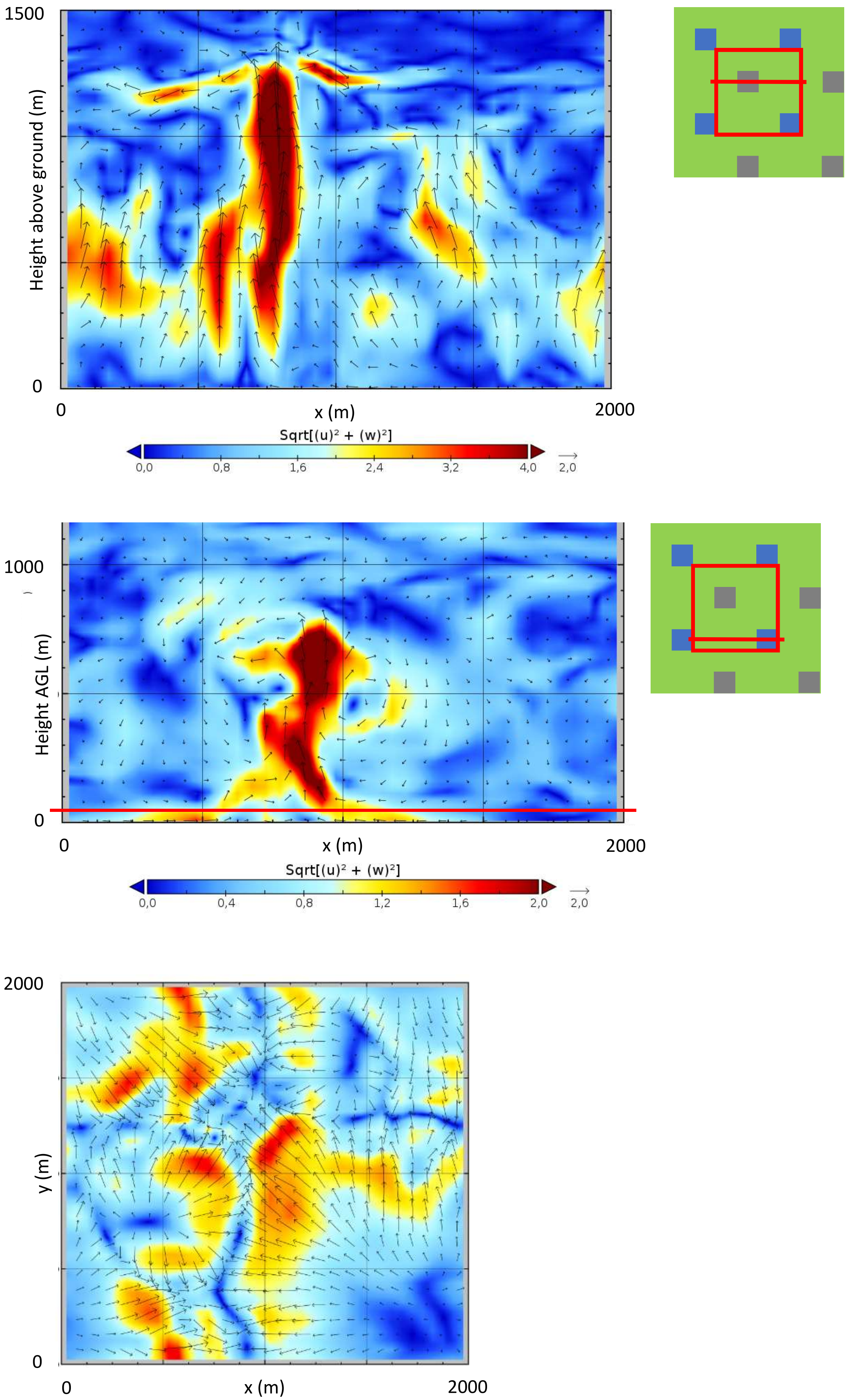

Fig. 17: Flow pattern after 48 h. Top: vertical velocity field in section through asphalt and grass. Middle: vertical velocity field, section through grass and water, scale changed. Bottom: horizontal velocity field at 37.5 m height, same velocity scale.

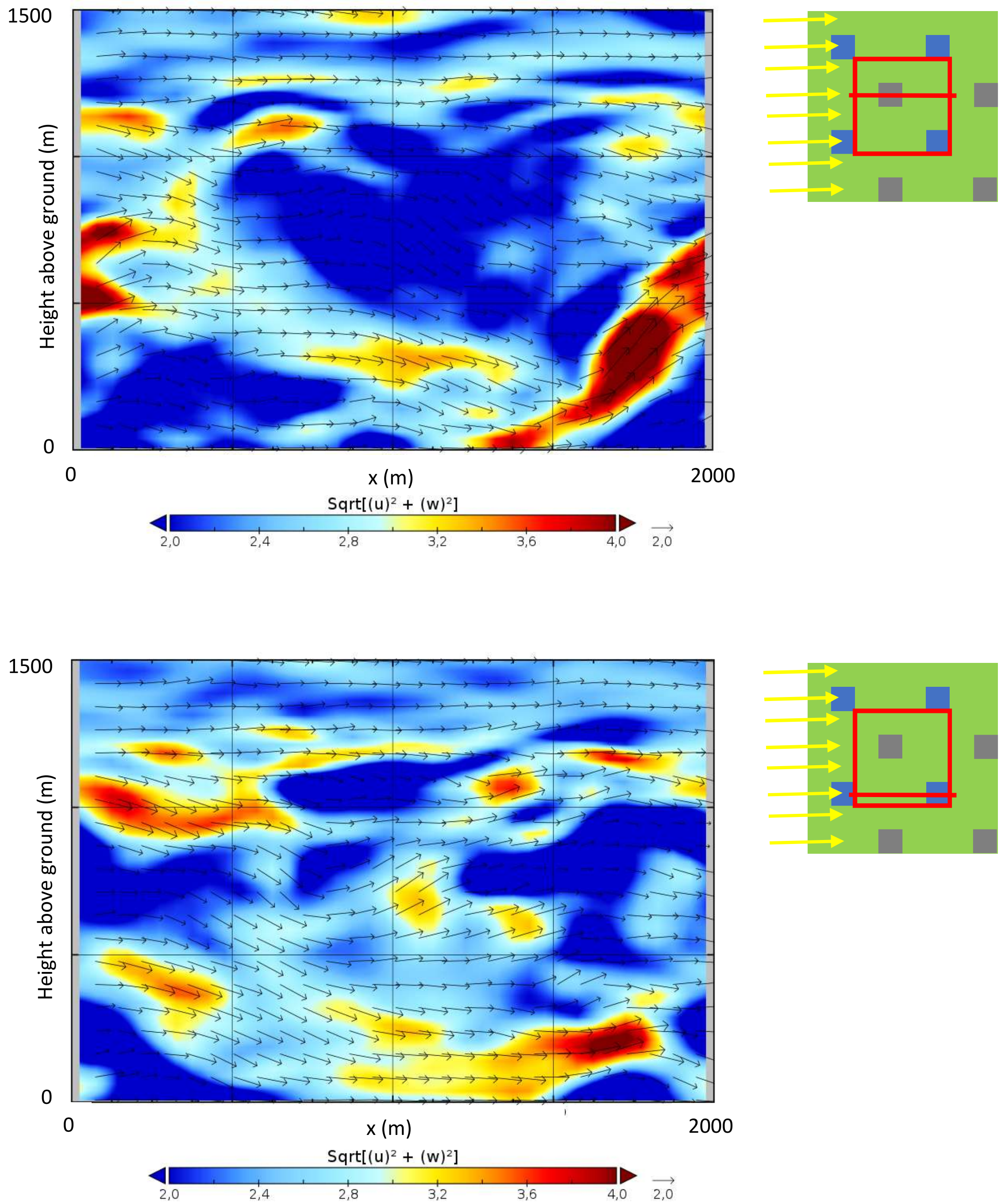

Fig. 18: Wind disrupts thermal columns into bubbles. Top: Vertical section parallel to the wind through asphalt area. Bottom: through water area.

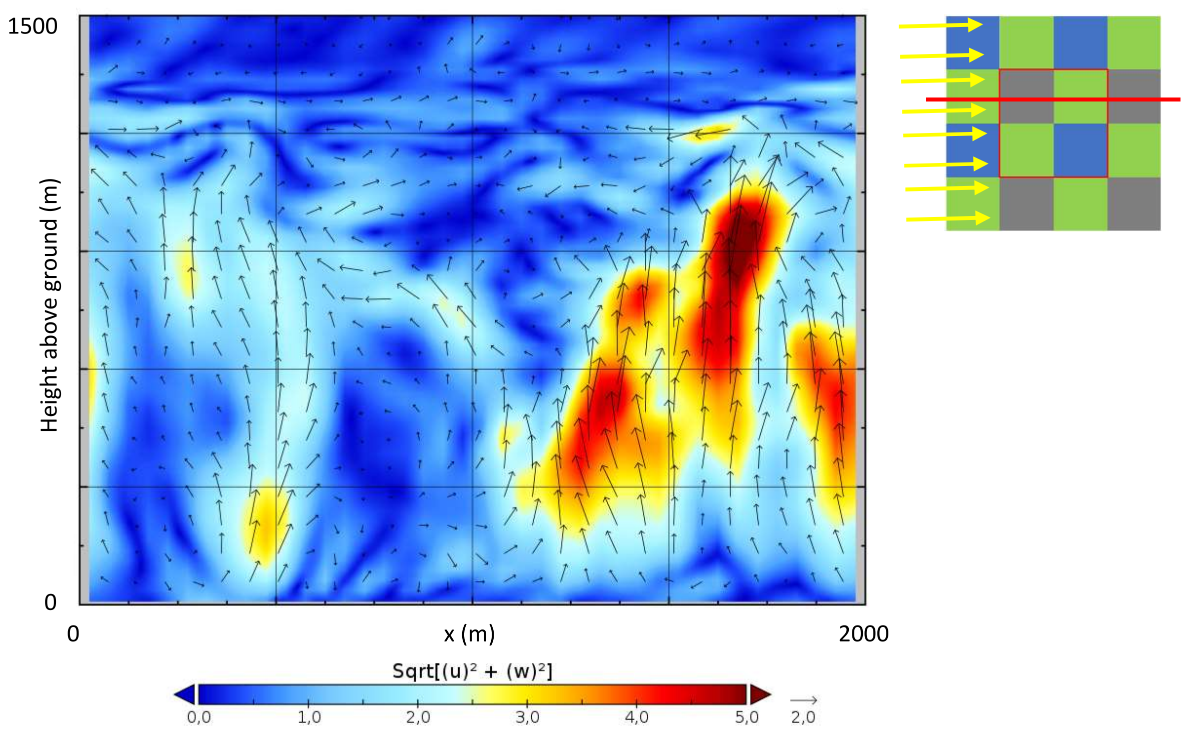

Fig. 19: Vertical flow field section through asphalt region after subtraction of the mean wind. The thermal bubbles are oriented vertically and drift with the wind. The velocity vectors in updraft regions are oriented vertically. Inclined thermals are not observed.

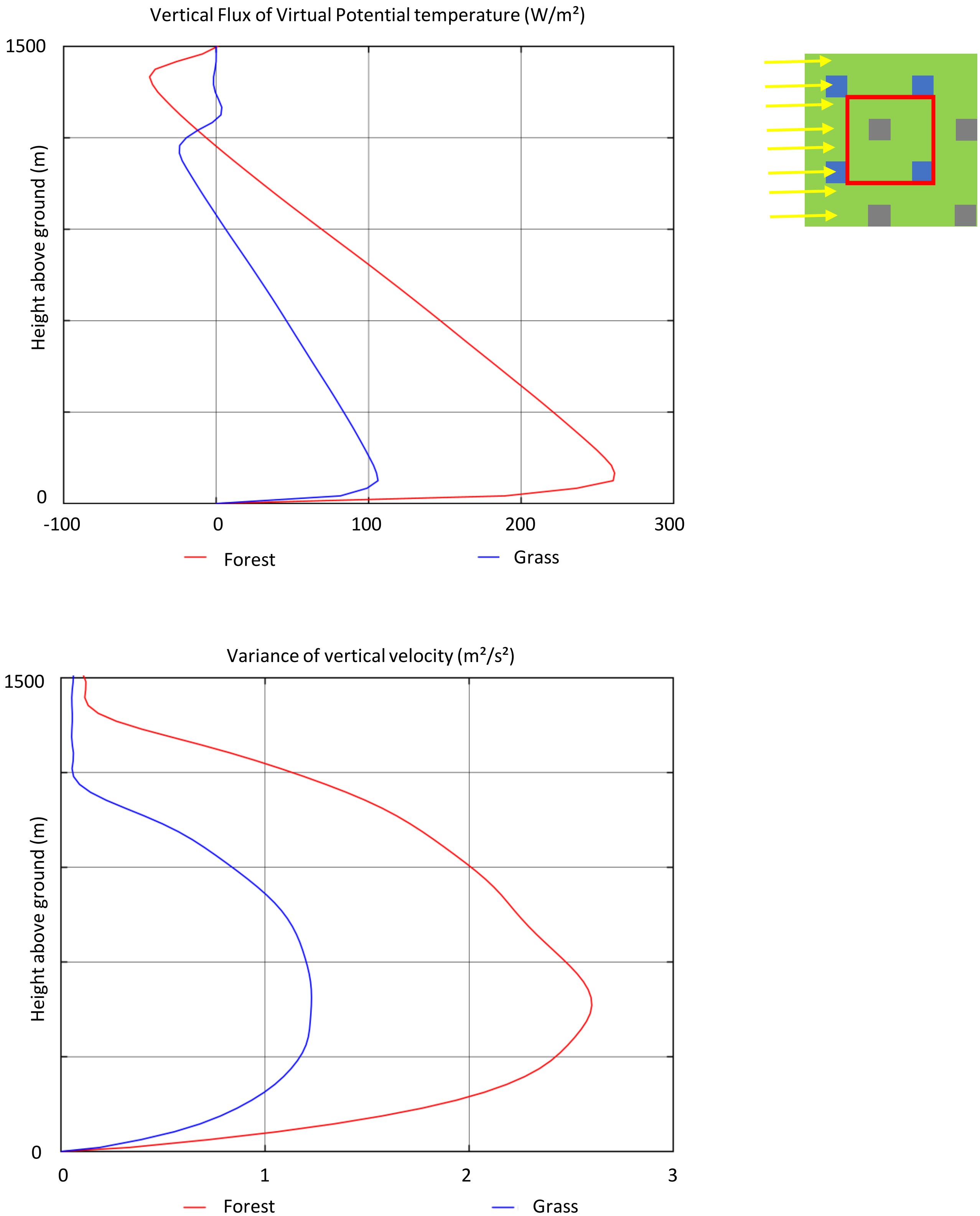

Fig. 20: **In a "forest scenario", green surfaces are covered with an interrupted forest type of vegetation (type 18) instead of grass. The top diagram shows that virtual potential temperature flux and inversion height are both much higher in the "forest scenario". The bottom diagram is the resulting thermal strength, the variance of vertical velocity, which is also higher above forest.**

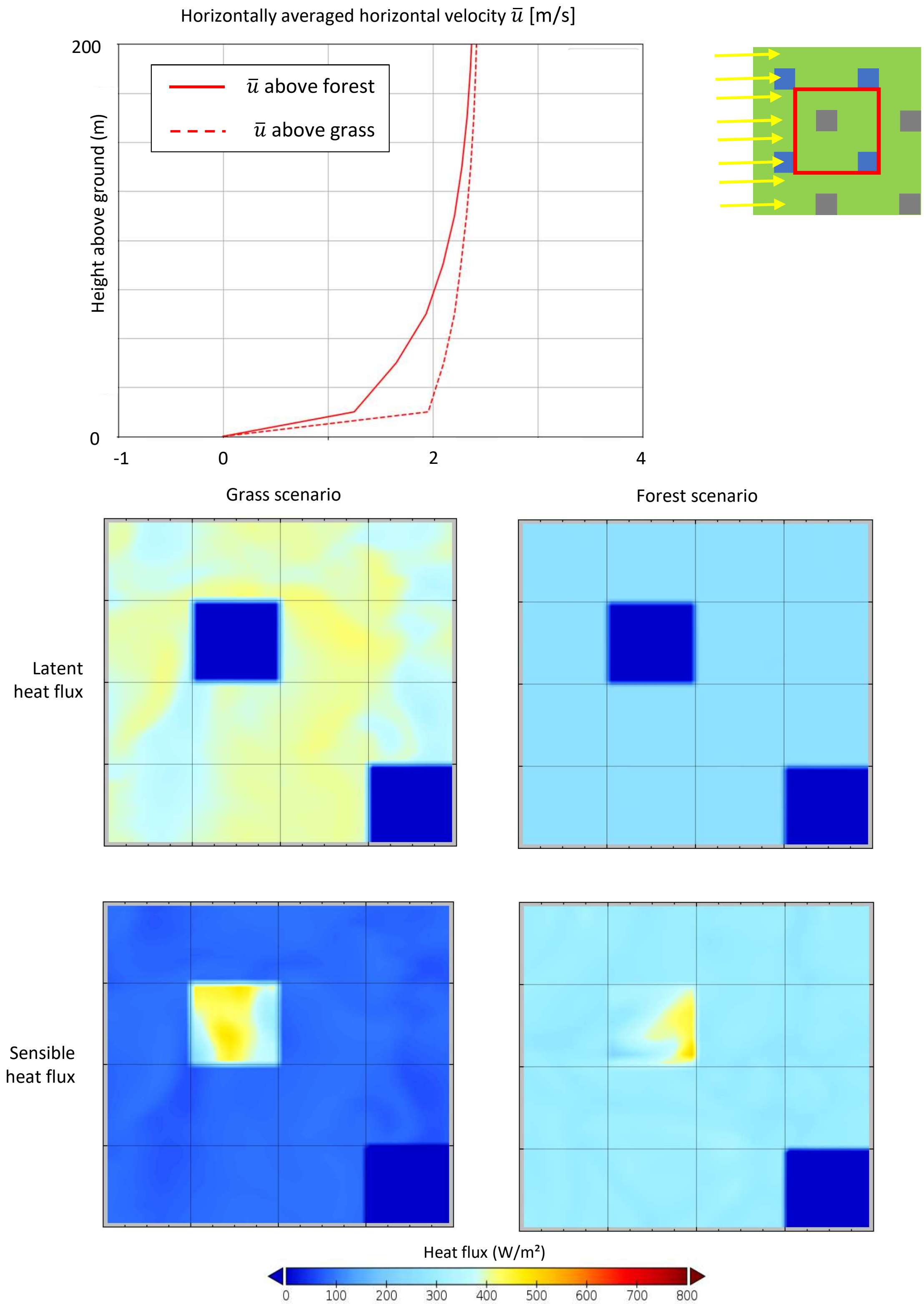

Fig. 21: Top: Root cause is the higher gradient of the mean horizontal velocity near the ground above grass (dashed line) and above forest (solid line). Bottom: Comparison of latent heat flux and sensible heat flux (rows) for the grass and the forest scenario (columns). The differences above asphalt and water are low, but latent heat flow is significantly higher above grass, and sensible heat flow significantly higher above forest.

Appendix
Animations of Thermal Simulations

Animated visualizations of the Large Eddy Simulation of thermal development in the different scenarios described in the preceding sections are provided (see hyperlinks below), and discussed.

The 3D movies show thermals developing over horizontally homogeneous flat terrain as in Fig. 4 top left. To improve spatial awareness, the camera is rotated around the scene. The *xyz* orientation is indicated in the image by the red-green-blue tripod. Running time is the last 30 minutes of a 3 hour simulation, when statistical stationarity is achieved, with snapshots every 10 s. The general frame rate is 10 fps, so the time lapse rate is 100x.

Movie 1

MP4 file: `movie1.mp4`

The movie shows cool (compared to the respective horizontal average) blue spots, moving over the heated surface, converging with other cells, concentrating and forcing up warm air, which is accelerated vertically by this convergence and buoyancy. Temperature differences diminish with increasing height, and disappear at quite low height, as in Fig. 5.

Movie 2

MP4 file: `movie2.mp4`

The movie shows an enlarged view of the finer nested grid data near the heated surface, with time lapse rate 10 fps only.

Movie 3

MP4 file: `movie3.mp4`

The movie shows buoyancy, coloured magenta if positive and green if negative, developing while temperature excess vanishes, and being present through a major portion of the boundary layer. Green air parcels (negative buoyancy) near the inversion are moving downwards, so their specific kinetic energy vanishes, reducing their speed.

Movie 4

MP4 file: `movie4.mp4`

The movie shows specific kinetic energy, coloured yellow to red, developing at and above regions with high buoyancy.

Movie 5

MP4 file: `movie5.mp4`

This movie shows thermals above inhomogeneous terrain and without wind, with snapshots every 60 s. This is the scenario from Fig. 17. It starts with the camera looking North and slowly rotating counter clockwise around the scene. Visibility is cut from the inversion and above. Through the first couple of seconds virtual potential temperature difference from the horizontal mean is shown, being highest above the asphalt and lowest above water. Virtually warmer air parcels can be observed higher than above a homogenous surface. Later visibility of buoyancy ptflux is switched on, in the last phase visibility of dpt is switched off and of specific kinetic energy is switched on. Positive buoyancy is observed directly above the surface and even above highest virtual temperature excess. The thermals big and strong enough to be useable for soaring pulsate even in this quasi stationary environment, build on top of high buoyancy and penetrate into the inversion. Around the penetration region, a green ring of air with negative buoyancy builds, but not reaching far down.

Movie 6

MP4 file: `movie6.mp4`

This movie shows exactly the same scenario as in Movie 5, except for a geostrophic wind in the free atmosphere from the West. This flow and momentum are mixed down into the boundary layer, only near the surface the wind slightly turns counter clockwise to WSW because of surface friction. Virtually warmer air at the surface is concentrated again on asphalt, above it is less concentrated than without wind, and advected with the wind. Interestingly, structures with high buoyancy are oriented vertically, while also being advected. The resulting zones of high specific kinetic energy are consequently also oriented vertically. Separate thermal bubbles follow each other in the wind direction (more the surface wind than the geostrophic wind direction!). The movie shows that thermals originate from the asphalt patches, but not necessarily the nearest ones.